Spin-photon interaction between a ruby crystal and a high-critical-temperature superconducting microwave cavity

Check for updates

Z. Velluire-Pellat ⑩, E. Maréchal ⑩, C. Feuillet-Palma ⑩ & N. Bergeal ⑩ ✉

High-spin systems in molecules and inorganic solids hold significant potential for advancing quantum information storage and processing technologies, owing to their multilevel structure. However, the dynamics of spin-photon interactions in these systems remain underexplored in practical device settings. Here we investigate the quantum properties of an $S = 3/2$ spin ensemble in a ruby crystal embedded in a high-T_c superconducting microwave cavity. Using electron spin resonance techniques, we measure the coupling strength between the quantized electromagnetic mode of the cavity and the spin ensemble across a broad temperature range and for various crystal axis orientations relative to the applied magnetic field. The coupling strength, governed by thermal polarization of the spins and quantum mechanical transition probabilities, shows quantitative agreement with theoretical predictions based on spin Hamiltonian diagonalization and electromagnetic simulations of the cavity mode. These findings establish impurity spins in solids as controllable multilevel quantum systems and provide critical insights into the factors influencing spin-cavity interactions. This work opens new avenues for optimizing quantum information processing and developing versatile quantum technologies based on high-spin systems.

Over the past decade, quantum information processing has emerged as a revolutionary paradigm, offering unprecedented computational power and secure communication channels[1]. A compelling strategy for building a quantum processor involves developing hybrid quantum systems, where information is processed using qubits that are separated from dedicated memory registers, i.e., quantum memories[2]. Among the possible candidates, electron spin impurities in inorganic solids[3], such as diamond nitrogen-vacancy centers[4,5], donor spins in silicon[6] or rare earth ions embedded in crystals[7,8], offer several advantages for implementing quantum memories[9,10].

In the canonical framework, quantum information is encoded in qubits –the quantum analog of classical bits– by isolating two specific energy levels within a quantum system[1]. However, the underlying multilevel nature of various quantum platforms represents a powerful resource for quantum computation. Qudit technology, which involves d-level quantum digits ($d > 2$), provides a larger state space for storing and processing information, thereby offering significant potential for improvements in algorithm efficiency and computational power[11,12]. Quantum information processing with qudits has been experimentally demonstrated in a variety of systems, including superconducting circuits[13,14], trapped ions[15], molecular magnets[16], and nuclear spins[17–19].

In this context, high-electronic spins ($S > 1/2$) in molecules and inorganic solids present an interesting alternative for quantum applications. These systems offer several advantages : (i) relatively long coherence times, which are crucial for preserving quantum information[20,21]; (ii) transition energies that typically fall within the microwave frequency range ($\Delta E \sim g\mu_B B$), where conventional solid-state qubits operate[22,23]; and (iii) the ability to coherently manipulate spin states using Electron Spin Resonance (ESR) techniques in cavity. In practice, superconducting cavities are often employed due to their low conducting losses, which results in higher quality factors[24,25]. These cavities enable strong coupling to be achieved between a microwave cavity field and the spins in a highly cooperative regime[3]. However, the use of superconducting materials limits the range of magnetic fields that can be applied, as the field must remain below the superconducting critical field. This limitation can be mitigated by using magnetically resilient superconducting materials, such as NbTi[26], NbN[27], or granular aluminum[28]. Moreover, high-T_c superconducting cavities[29–31] offer extended operating ranges in both magnetic field and temperature compared to their low-T_c counterparts.

In this work, we investigate the interaction between the fundamental electromagnetic mode of a high-Tc superconducting cavity and an $S = 3/2$ spin ensemble, specifically Cr^{3+} spin impurities embedded in a ruby

Laboratoire de Physique et d'Étude des Matériaux, ESPCI Paris, Université PSL, CNRS, Sorbonne Université, Paris, France. ✉e-mail: nicolas.bergeal@espci.fr

crystal. Using Electron Spin Resonance (ESR) technique, we quantify the spin-cavity coupling and the spin decay rate over an extended temperature range that spans different thermal occupation regimes of the spin energy levels. Our analysis reveals a complex temperature dependence of the coupling, driven by the interplay between thermal polarization of the spins and quantum mechanical transition probabilities, governed by Fermi's golden rule. Furthermore, by adjusting the magnetic field orientation relative to the crystal axis, we successfully modulate the number of active transitions in the quantum system, from two to four transitions within this study. Additionally, we theoretically analyze the coupling within the Tavis–Cummings model framework[32,33], calculating the spatial distribution of the magnetic field in the ruby crystal generated by the zero-point fluctuations of the microwave current within the cavity. This allows us to evaluate the contribution of a single spin at any location and predict the temperature-dependent coupling behavior for the spin ensemble. While the absolute values of the measured coupling remain modest, our methodology provides a systematic approach for investigating spin-photon interactions in circuit quantum electrodynamics. The agreement between our model and experimental results highlights the relevance of this approach and suggests that high-spin systems warrant further exploration for their potential role in quantum technologies.

Results

Sample and experimental setup

Ruby is a corundum (Al_2O_3) crystal, whose distinct red hue results from chromium dopants that replace some of the aluminum atoms. It can be manufactured artificially with a relatively low concentration of chromium, typically on the order of 0.1%, and was originally considered for its applications in lasers[34] and masers[35]. When a chromium atom substitutes for an aluminum atom, it transfers three electrons to the six O^{2-} neighbor ions to form Cr^{3+} ions with electronic configuration $[Ar]3d^3$. The three valence electrons occupy the t_{2g} orbitals ($3d_{xy}, 3d_{xz}, 3d_{yz}$), which are lower in energy than the e_g ones in the octahedral crystal field. The spin states associated with the Cr^{3+} ground state, which have a quenched orbital angular momentum, can be treated as those of an effective $S = 3/2$ spin. The crystal field influences the electron spins indirectly through spin-orbit coupling, resulting in a splitting of approximately 11.5 GHz between the energy levels associated with a magnetic quantum number $m = \pm3/2$ at lower energy and $m = \pm1/2$ at

higher energy. This well-defined spin structure makes ruby an attractive platform for performing ESR experiments. In particular, superconducting coplanar waveguides and cavities have been used to probe spin-photon coupling in Cr^{3+} spin ensembles[24,36]. In the following, we consider the experimental configuration presented in Fig. 1. A piece of ruby is placed in contact with a $\lambda/2$ - $YBa_2Cu_3O_{7-x}$ superconducting coplanar waveguide cavity[31] such that its crystallographic c-axis, denoted the z-axis, lies in the sample plane. Additionally, a small amount of 2,2-diphenyl-1-(2,4,6-trinitrophenyl) hydrazyl (DPPH) powder is also placed in contact with the cavity and serves as an $S = 1/2$ ESR standard for magnetic field calibration. The superconducting cavity has a resonant frequency $f_0 = \frac{\omega_0}{2\pi} \simeq 5.5$ GHz and a quality factor $Q \approx 8500$ at zero external magnetic field (Fig. 1c). It generates a microwave AC magnetic field, suitable for inducing ESR transitions between the Cr^{3+} spin states under a Zeeman magnetic field **B** applied along the z_0 direction[37]. The cavity was integrated into a microwave setup within a dilution refrigerator to measure its transmission $S_{21}(\omega)$ at temperatures ranging from 30 mK to 16 K. All the measurements were performed with an average photon number in the cavity of approximately 2×10^6. Detailed information about the setup and measurement parameters is provided in the "Methods" section.

Spin Hamiltonian

The spin Hamiltonian for the ground state of Cr^{3+} ions in the Al_2O_3 lattice results from the contributions of two Zeeman terms and a crystal field term[38–40]:

$$\mathcal{H}_s = g_\perp \mu_B [B_x S_x + B_y S_y] + g_\parallel \mu_B B_z S_z + D[S_z^2 - S(S+1)/3],$$

(1)

where $g_\parallel = 1.9817$ and $g_\perp = 1.9819$ are the in-plane and out-of-plane g-factors, respectively, μ_B is the Bohr magneton, and D represents the crystalline zero-field splitting ($2D/h = 11.493$ GHz). $B_{i=x,y,z}$ are the components of the magnetic field, and $S_{i=x,y,z}$ are the spin operators in the corresponding directions (Supplementary Note 2). Given the marginal difference between the values of $g_\parallel$ and $g_\perp$, we will consider the average isotropic g-factor, $\bar{g} = (g_\parallel + 2g_\perp)/3$, in the following. In Eq. (1), we have chosen the quantization axis (z-axis) coinciding with the natural crystal symmetry axis (c-axis) to make the crystal field term diagonal. The magnetic field is applied along the z_0 direction and oriented at an angle θ with respect

Fig. 1 | Description of the Electron Spin Resonance experiment. a Schematic description of the $\lambda/2$ - $YBa_2Cu_3O_{7-x}$ superconducting coplanar waveguide cavity with the ruby and 2,2-diphenyl-1-(2,4,6-trinitrophenyl) hydrazyl (DPPH) pellet[31]. The ruby crystal is glued on the sample using a thin layer of vacuum grease (not represented here). The (x_0, y_0, z_0) coordinate system, associated with the cavity, is obtained by a rotation of angle θ of the (x, y, z) system around the y axis, such that the Zeeman magnetic field **B** is applied along the z_0 axis. **b** Distribution of the normalized amplitude of the microwave magnetic field B_{ac}/B_{max}, in the cavity, shown in color scale along cuts 1 and 2. **c** Transmission of the cavity $S_{21}(\omega)$ in dB scale (blue dots) centered on the resonance frequency f_0 fitted by a Lorentzian curve providing a quality factor $Q \approx 8500$ (red full line).
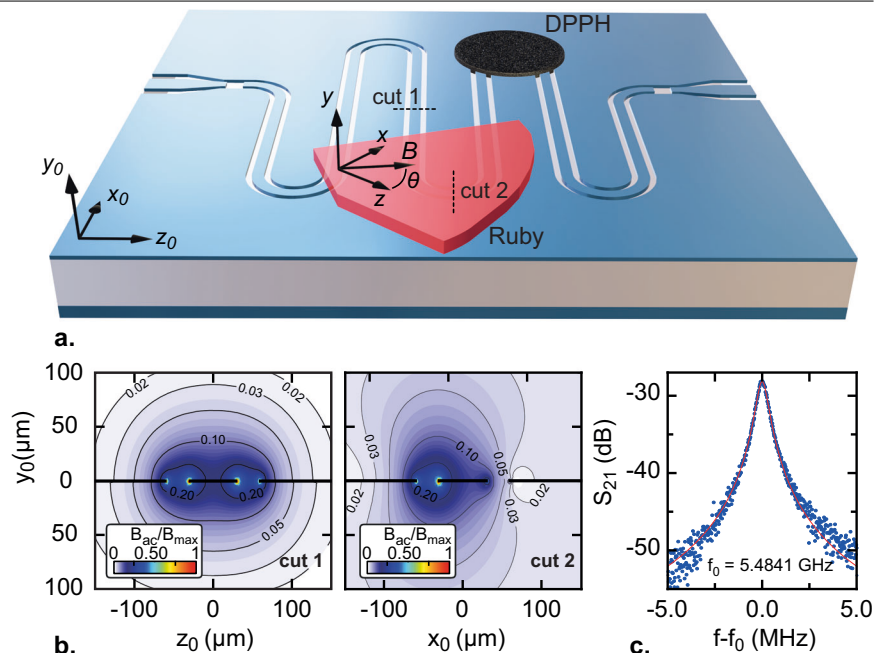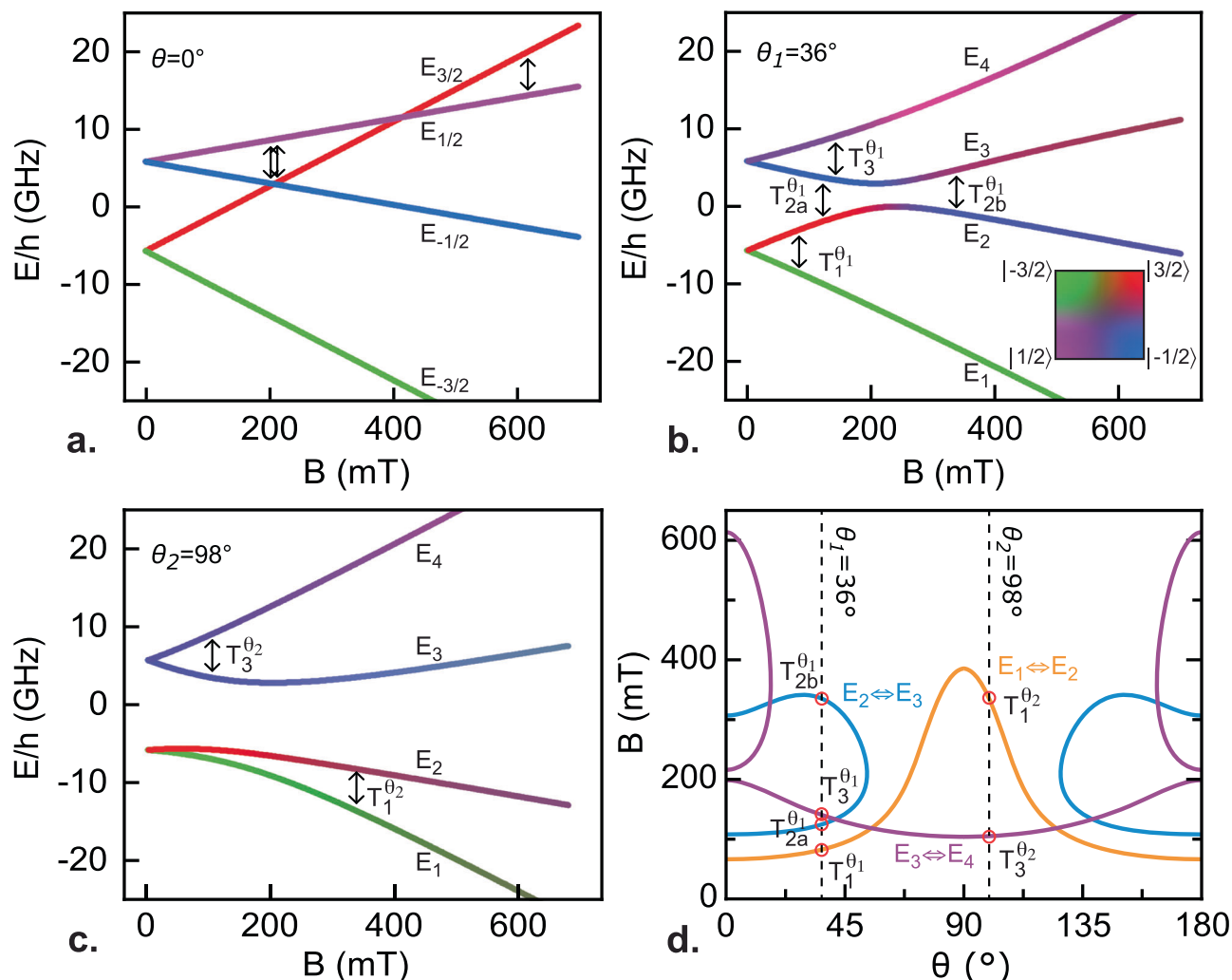
Fig. 2 | Spin energy levels and Electron Spin Resonance (ESR) transitions experimentally accessible. Magnetic field dependence of the spin energy levels for $\theta = 0°$ (**a**), $\theta = 36°$ (**b**), and $\theta = 98°$ (**c**). The spin character $|m\rangle$ is indicated by the color scale in (**b**). Eigenenergies are labeled in ascending order, and arrows indicate authorized ESR transitions in our cavity with resonance frequency $f_0 = 5.5$ GHz. **d** Isofrequency plot in the magnetic field-angle plane for observable transitions at $f_0 = 5.5$ GHz. Red circles indicate the transition at the angles $\theta = 36°$ and $\theta = 98°$ that are addressed experimentally.

to the z-axis (Fig. 1a), such that $B_x = B \sin \theta$, $B_y = 0$, and $B_z = B \cos \theta$. At zero magnetic field, the Hamiltonian eigenstates are those of the S_z operator, $|m\rangle = |3/2\rangle, |1/2\rangle, |-1/2\rangle, |-3/2\rangle$, and the spin states consist of two doublets, $\{|\pm 3/2\rangle\}$ with energy $E_{|\pm 3/2\rangle} = -D/h$ and $\{|\pm 1/2\rangle\}$ with energy $E_{|\pm 1/2\rangle} = +D/h$. In a finite magnetic field, the eigenenergies E_n and eigenstates $|\phi_n\rangle$ of $\mathcal{H}_s$ depend on the angle θ and are obtained by diagonalizing the following matrix Hamiltonian:

$$\hat{\mathcal{H}}_s = \begin{bmatrix} 3/2\alpha - D & \sqrt{3}\beta/2 & 0 & 0 \\ \sqrt{3}\beta/2 & \alpha/2 + D & \beta & 0 \\ 0 & \beta & -\alpha/2 + D & \sqrt{3}\beta/2 \\ 0 & 0 & \sqrt{3}\beta/2 & -3\alpha/2 - D \end{bmatrix} \quad (2)$$

where $\alpha = \bar{g}\mu_B B \cos \theta$ and $\beta = \bar{g}\mu_B B \sin \theta$. A transition between two levels E_k and E_l can occur if the ESR condition $|E_k - E_l| = \hbar\omega_0$ is met. The transition probability between these two levels is given by Fermi's golden rule and is proportional to the transition matrix element $W_{k,l} = \langle \phi_k | W | \phi_l \rangle = \bar{g}\mu_B \langle \phi_k | \mathbf{B}_{ac}.\mathbf{S} | \phi_l \rangle$ with $\mathbf{B}_{ac}$ being the local AC magnetic field generated in the ruby at the spin position, by the microwave current in the cavity. The $W_{k,l}$ matrix element ensures that the selection rule for magnetic dipole transitions, $\Delta m = \pm 1$, is satisfied.

Transitions and spin-cavity coupling

Figure 2 shows the evolution of the spin energy levels with magnetic field for three different angles, $\theta = 0°$, $\theta = 36°$, and $\theta = 98°$. In the trivial case $\theta = 0°$ (panel a), the Hamiltonian is diagonal and the Zeeman effect splits the two doublets into four non-degenerate states. For this angle only, the basis vectors $\{|m\rangle\}$ are the eigenstates of the system, regardless of the amplitude of the magnetic field. Three transitions can, in principle, be observed with our cavity: $E_{|1/2\rangle} \Longleftrightarrow E_{|3/2\rangle}$ twice and $E_{|-1/2\rangle} \Longleftrightarrow E_{|1/2\rangle}$ (see arrows on Fig. 2a). For any angle $\theta \neq 0$, the spin states hybridize, and the eigenstates of $\hat{\mathcal{H}}_s$ become linear combinations of all basis vectors with non-zero a_n coefficients, $|\phi_{n=1,2,3,4}\rangle = a_{n,3/2}|3/2\rangle + a_{n,1/2}|1/2\rangle + a_{n,-1/2}|-1/2\rangle + a_{n,-3/2}|-3/2\rangle$. As a result, the transition matrix element $W_{k,l}$ is always finite, and all the transitions satisfying the ESR condition can take place with a non-zero probability. In Fig. 2b and c, the absolute values of the a_n coefficients are encoded in a color scale to emphasize the hybridization of the levels for the angles $\theta_1 = 36°$ and $\theta_2 = 98°$ that are studied experimentally and will be discussed in the following. For θ_1, four ESR transitions are expected: the transition $T_1^{\theta_1}$ ($E_1 \Leftrightarrow E_2$), the transitions $T_{2a}^{\theta_1}$ and $T_{2b}^{\theta_1}$ ($E_2 \Leftrightarrow E_3$) at two different magnetic fields, and the transition $T_3^{\theta_1}$ ($E_3 \Leftrightarrow E_4$). For θ_2, only two ESR transitions are expected: transition $T_1^{\theta_2}$ ($E_1 \Leftrightarrow E_2$) and transition $T_3^{\theta_2}$ ($E_3 \Leftrightarrow E_4$). The ESR transitions observable with our superconducting cavity can be more clearly visualized by plotting the isofrequency lines at

$f_0 = 5.5$ GHz as a function of the magnetic field B and the angle θ (Fig. 2d). Given the symmetry of the ruby crystal, the plot is π-periodic and symmetric around $\pi/2$. The two dashed lines, which indicate the angles $\theta_1 = 36°$ and $\theta_2 = 98°$, intercept the isofrequency lines at the transitions discussed above (red circles). Figure 2d shows that the angle θ is a tunable parameter, which controls the number of active transitions in the quantum system, ranging from two transitions ($\theta \gtrsim 53°$), to four transitions ($17° \lesssim \theta \lesssim 53°$), and up to six transitions ($\theta \lesssim 17°$).

Close to the transition between two energy levels $E_k \Leftrightarrow E_b$, the coupling between a single Cr^{3+} spin and a quantized electromagnetic mode in the cavity can be treated within the framework of the Jaynes–Cummings Hamiltonian[41],

$$\mathcal{H}_{JC} = \hbar\omega_{kl}\sigma^+\sigma^- + \hbar\omega_0 a^\dagger a + \hbar\Omega(\mathbf{r_i})(a\sigma^+ + a^\dagger\sigma^-), \quad (3)$$

where $\omega_{kl} = |E_k - E_l|/\hbar$ is the transition frequency between states $|\phi_k\rangle$ and $|\phi_l\rangle$. σ^+ and σ^- are the spin ladder operators acting in the subspace of dimension two generated by $|\phi_k\rangle$ and $|\phi_l\rangle$, and $a^\dagger$ and a are the bosonic creation and annihilation operators of the electromagnetic mode. The spin-cavity coupling constant in Eq. (3) is $\Omega(\mathbf{r_i}) = \bar{g}\mu_B|\langle\phi_k|\mathbf{b_0}(\mathbf{r_i}).\mathbf{S}|\phi_l\rangle|$, where $\mathbf{b_0}(\mathbf{r_i})$ is the magnetic field generated by the zero-point fluctuations of the microwave current in the cavity, at the spin location $\mathbf{r_i}$. To describe an ensemble of N spins, Ω must be replaced by an effective coupling constant $\bar{\Omega}$, which accounts for the contribution of each spin at position $\mathbf{r_i}$, and for the thermal occupation of the energy levels involved in the transition. For the $E_k \Leftrightarrow E_l$ transition, the effective coupling reads[42],

$$\bar{\Omega}(T) = \bar{g}\mu_B\sqrt{n_{k,l}(T)\Sigma_{i=1}^N|\langle\phi_k|\mathbf{b_0}(\mathbf{r_i}).\mathbf{S}|\phi_l\rangle|^2}, \quad (4)$$

where $n_{k,l}(T) = |e^{-E_k/k_B T} - e^{-E_l/k_B T}|/\Sigma_j e^{-E_j/k_B T}$ is a thermal polarization factor derived from Boltzmann statistics (Supplementary Note 3). Equation (4) leads to a $\sim\sqrt{N}$ enhancement of the effective coupling with respect to that of a single spin as predicted in the Tavis–Cummings model for collective coupling effects[32,33,43].

ESR measurements

We now present the experimental results obtained with the configuration described in Fig. 1a. In this first experiment, the Ruby sample was placed at an unknown angle θ with respect to the magnetic field. Figure 3a shows the magnetic field dependence of $S_{21}(\omega)$ in dB scale (up panel) and its maximum value (down panel) measured at $T = 186$ mK. In addition to the DPPH line, which is used to calibrate the magnetic field, four transitions associated with the Cr^{3+} spin levels are observed at magnetic fields $B = 83 \pm 2$ mT, 122.5 ± 2 mT, 143.5 ± 2 mT, and 338.5 ± 2 mT. According to the isofrequency transition lines in Fig. 2d, such configuration can unambiguously be associated with an angle $\theta_1 = 36 \pm 2°$, and corresponds to the transitions $T_1^{\theta_1}$, $T_{2a}^{\theta_1}$, $T_{2b}^{\theta_1}$, and $T_3^{\theta_1}$, respectively (Fig. 2b). Note that two $E_2 \Leftrightarrow E_3$ transitions are observed ($T_{2a}^{\theta_1}$ and $T_{2b}^{\theta_1}$) due to the non-monotonous magnetic field dependence of the energy levels, which satisfy the ESR condition twice (Fig. 2b). In a second experiment, the ruby sample was rotated to investigate the ESR transitions in the right part of the isofrequency lines plot (Fig. 2d). An example of the magnetic field dependence of $S_{21}(\omega)$ and its maximum at $T = 186$ mK is shown in Fig. 3b. Two Cr^{3+} spin transitions are visible at magnetic fields $B = 106 \pm 2$ mT ($T_3^{\theta_2}$) and 345 ± 2 mT ($T_1^{\theta_2}$), which corresponds to an angle $\theta_2 = 98 \pm 2°$ (Fig. 2c, d).

To further analyze our ESR data, we consider the expression of the cavity transmission in the presence of a spin ensemble, near the $E_k \Leftrightarrow E_l$ transition[44]

$$S_{21}(\omega, B) \simeq \frac{\omega_0/Q_c}{\omega_0/Q + 2i(\omega_0 - \omega) + \frac{2\bar{\Omega}^2}{i(\omega_{kl}(B)-\omega)+\gamma_s}}, \quad (5)$$

where γ_s is the decay rate of the spin ensemble, Q is the total quality factor of the cavity, and Q_c is the coupling quality factor of the cavity to its environment. For limited damping ($\gamma_s \lesssim \bar{\Omega}$), $S_{21}(\omega, B)$ features two resonance frequencies, which correspond to the usual vacuum Rabi splitting

$$\omega_\pm = \omega_0 + \frac{\Delta}{2} \pm \frac{\sqrt{\Delta^2 + 4\bar{\Omega}^2}}{2}, \quad (6)$$

where $\Delta(B) = \omega_{kl}(B) - \omega_0$ is the detuning. In the opposite limit of strong damping ($\gamma_s \gtrsim \bar{\Omega}$), $|S_{21}(\omega)|^2$ can be approximated by a Lorentzian curve with quality factor[24]

$$Q_s = \frac{\Delta^2 + \gamma_s^2}{2\bar{\Omega}^2\gamma_s + \omega_0/Q(\Delta^2 + \gamma_s^2)}\omega_0 \quad (7)$$

While $Q_s \simeq Q$ at large detuning, it decreases to $Q_s \simeq \frac{\gamma_s\omega_0}{2\bar{\Omega}^2}$ at spin resonance due to the combined effects of the spin-photon coupling rate and the spin decay rate.

As seen in Fig. 3a, b, the cavity transmission exhibits some anticrossings characteristic of spin-photon interaction close to the ESR transitions. However, for most of the transitions the damping is too strong for a direct comparison of the experimental data with Eq. (5). Nevertheless, in this regime, the coupling constant $\bar{\Omega}$ and the spin decay rate γ_s can be directly extracted from experimental data by a fit to Eq. (7). We therefore apply the following procedure. For each observed transition, the detuning $\Delta(B) = \omega_{kl}(B) - \omega_0$ is first calculated from the magnetic field dependence of the energy levels shown in Fig. 2. Next, we determine the quality factor of the cavity Q_s from a Lorentzian fit of $|S_{21}(\omega)|^2$ as a function of the detuning for all the experimentally investigated temperatures. Examples of Q_s evolution with Δ across the various ESR transitions are shown in Figs. 4 and 5 for angles θ_1 and θ_2, respectively, at selected temperatures. Finally, by fitting the $Q_s(\Delta)$ curves to the theoretical model of Eq. (7) (solid lines in Figs. 4a–d and 5a, b), we extract the effective coupling constant $\bar{\Omega}$ and the spin decay rate γ_s. The close alignment of the experimental data with theoretical predictions validates our approach, though some transitions, such as $T_1^{\theta_1}$ transition (Fig. 5a), show higher uncertainty due to weaker transition amplitudes. To gain a
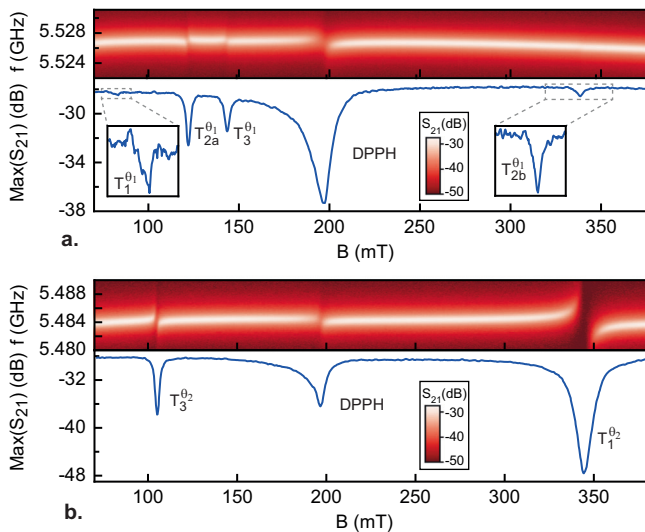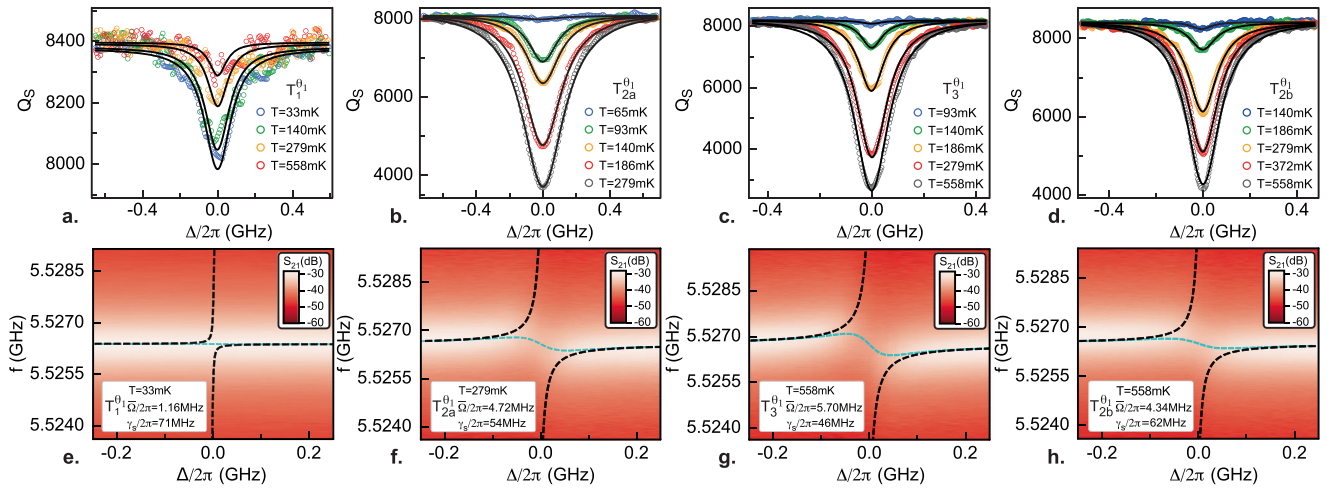
Fig. 3 | Electron Spin Resonance (ESR) transitions in the ruby sample. a Evolution of $S_{21}(\omega, B)$ in color scale (up) and of its maximum (down) with the magnetic field, at $T = 186$ mK, for $\theta_1 = 36°$. In addition to the 2,2-diphenyl-1-(2,4,6-trinitrophenyl) hydrazyl (DPPH) standard transition, the four transitions associated with Cr^{3+} ions are observed. The insets show close-up views of the $T_1^{\theta_1}$ and $T_{2b}^{\theta_1}$ transitions of weak amplitude. **b** Evolution of $S_{21}(\omega, B)$ in color scale (up) and of its maximum (down) with the magnetic field at $T = 186$ mK, for $\theta_2 = 98°$, showing the two transitions associated with Cr^{3+} ions.

Fig. 4 | Determination of the spin-cavity coupling for θ_1. Evolution of the cavity quality factor Q_s with detuning Δ at selected temperatures for the transitions $T_1^{\theta_1}$ (**a**), $T_{2a}^{\theta_1}$ (**b**), $T_3^{\theta_1}$ (**c**), and $T_{2b}^{\theta_1}$ (**d**). Symbols correspond to data extracted from the Lorenztian fit of $|S_{21}(\omega)|^2$ and full lines to the fit to Eq. (7). Magnitude of $S_{21}(\omega)$ in color scale as a function of detuning across the four Electron Spin Resonance (ESR)

transitions, $T_1^{\theta_1}$ (**e**), $T_{2a}^{\theta_1}$ (**f**), $T_3^{\theta_1}$ (**g**), and $T_{2b}^{\theta_1}$ (**h**). The light blue dashed lines represent the resonance frequency ω_r extracted from the simulations of Eq. (5) assuming the values of $\bar{\Omega}$ and γ_s determined by the fit of Q_s, while the black dashed lines represent the vacuum Rabi frequencies $\omega_{\pm}$ defined in Eq. (6).

Fig. 5 | Determination of the spin-cavity coupling constant for θ_2. Evolution of the cavity quality factor Q_s with detuning Δ at selected temperatures for the transitions $T_3^{\theta_2}$ (**a**) and $T_1^{\theta_2}$ (**b**). Symbols correspond to data extracted from the Lorenztian fit of $|S_{21}(\omega)|^2$ and full lines to the fit to Eq. (7). Magnitude of $S_{21}(\omega)$ in color scale as a function of detuning across the two Electron Spin Resonance (ESR) transitions, $T_3^{\theta_2}$ (**c**) and $T_3^{\theta_2}$ (**d**). The light blue dashed lines represent the resonance frequency ω_r extracted from the simulations of Eq. (5) assuming the values of $\bar{\Omega}$ and γ_s determined by the fit of Q_s, while the black dashed lines represent the vacuum Rabi frequencies $\omega_{\pm}$ defined in Eq. (6).
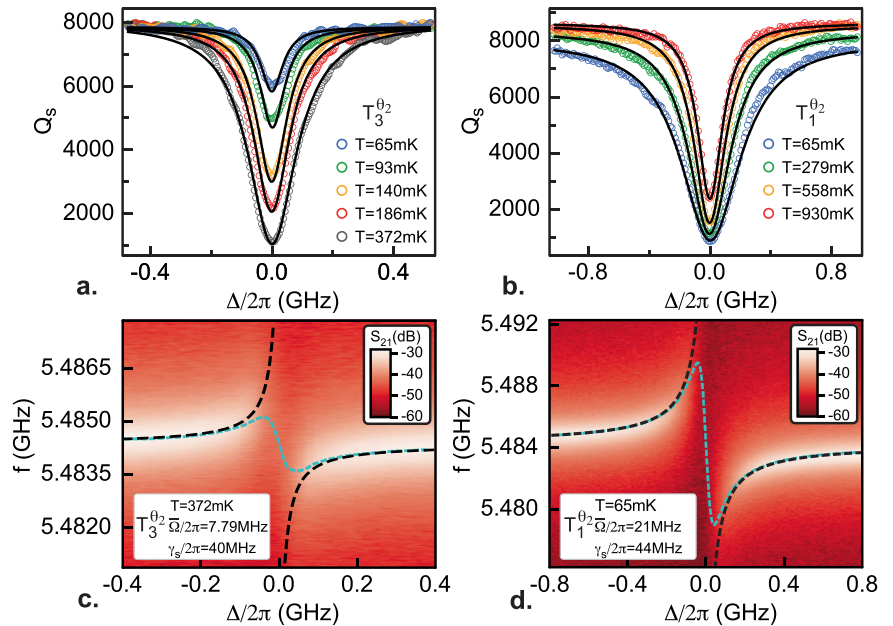
broader perspective in our analysis, we use the values of Q_s and γ_s determined by the fitting procedure to simulate $S_{21}(\omega)$ using Eq. (5) and extract the evolution of the cavity resonance frequency with detuning, $\omega_r(\Delta)$, across the ESR transitions. Examples for each transition are superimposed on color plots in Figs. 4e–h and 5c, d (light blue dashed lines) at temperatures corresponding to stronger coupling. While the $\omega_r(\Delta)$ line closely follows the maximum of $|S_{21}(\omega)|^2$ for the various transitions, it significantly departs from the vacuum Rabi frequencies $\omega_{\pm}$ (black dashed lines) as the transition is approached, which is expected in the strong damping regime. However, in the case of the $T_1^{\theta_2}$ transition at 65 mK, the anticrossing is more pronounced, and $\omega_r(\Delta)$ remains close to $\omega_{\pm}$ down to low detuning. The system enters a highly cooperative regime as $\bar{\Omega}/2\pi \approx 21$ MHz becomes comparable to $\gamma_s/2\pi \approx 44$ MHz, leading to a dimensionless cooperativity $C = \bar{\Omega}^2/(\kappa\gamma) \approx 15$, with $\kappa \approx \omega_0/Q$ denoting the cavity decay rate. Although $C \gg 1$, the system does not strictly satisfy the strong coupling condition, which also requires

$\bar{\Omega} > \gamma_s$. In the present regime, nearly every photon entering the cavity is coherently transferred into the spins; however, the spin relaxation rate is too fast to allow coherent re-emission of photons back into the cavity. The values of the spin relaxation rates for the different transitions are discussed in Supplementary Note 1.

Discussion

Figure 6 summarizes the temperature dependence of the coupling constant $\bar{\Omega}$ extracted from the fitting procedure for the different ESR transitions for the two angles, θ_1 (panel a) and θ_2 (panel b). To determine the theoretical coupling of the spin ensemble to a single photon, we estimate the zero-point fluctuation rms current in the cavity, I_{zpf}, by assuming that the zero-point energy is equally distributed between the cavity's inductor and capacitor, $\frac{1}{4}\hbar\omega_0 = \frac{1}{2}LI_{zpf}^2$ [42], where L is the inductance of the lumped equivalent RLC circuit[45]. Introducing the characteristic impedance of the cavity $Z_0 \simeq 50\,\Omega$,
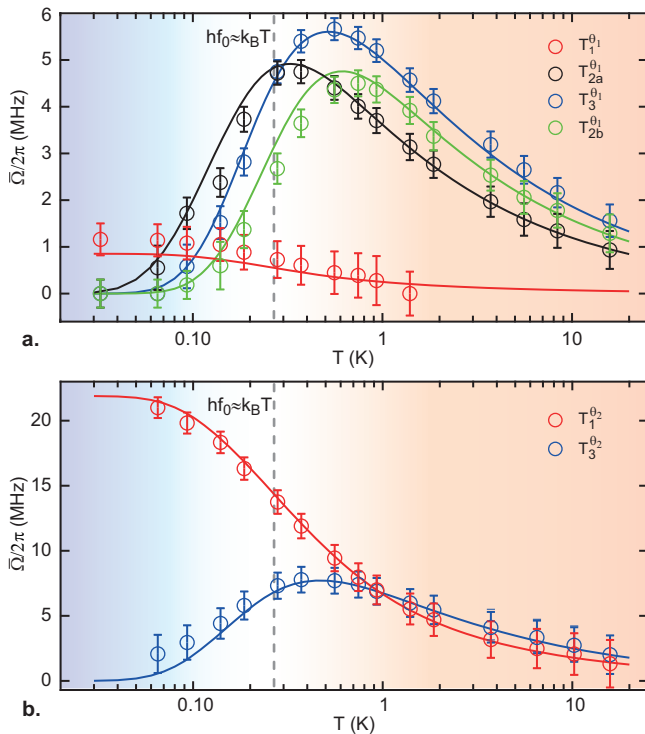
Fig. 6 | Temperature evolution of the coupling constant for the different transitions. a Temperature dependence of $\bar{\Omega}$ (symbols) for the four Cr^{3+} Electron Spin Resonance (ESR) transitions $T_1^{\theta_1}$, $T_{2a}^{\theta_1}$, $T_3^{\theta_1}$ and $T_{2b}^{\theta_1}$ at angle $\theta_1 = 36°$. The values of $\bar{\Omega}$ (symbols) are extracted from the fitting procedure of Q_s described in Fig. 4 with the corresponding error bars obtained from the fitting uncertainty. The data are then fitted to Eq. (4) (solid lines) using the simulated $\mathbf{b_0}$ magnetic field distribution shown in Supplementary Fig. 2 (see Supplementary Note 2). The best agreement is obtained for $\delta y_0 = 12\ \mu m$, corresponding to a global scaling factor of 0.65 for the fit of $\bar{\Omega}$. The dashed line, corresponding to $hf_0 \approx k_B T$ separates the thermal regime (right, shaded red) and the quantum regime (left, shaded blue). **b** Temperature dependence of $\bar{\Omega}$ (symbols) for the two Cr^{3+} transitions $T_3^{\theta_2}$ and $T_1^{\theta_2}$ at angle $\theta = 98°$ fitted to Eq. (4) (solid lines) using the simulated ac magnetic field distribution shown in Supplementary Fig. 2 (see Supplementary Note 2). The best agreement is obtained for $\delta y_0 = 6.5\ \mu m$, corresponding to a global scaling factor of 0.8 for the fit of $\bar{\Omega}$.

we obtain

$$I_{zpf} = \omega_0 \sqrt{\frac{\hbar\pi}{4Z_0}}. \tag{8}$$

For our $YBa_2Cu_3O_{7-\delta}$ cavity, with resonance frequency $f_0 \approx 5.5$ GHz, the zero-point fluctuation current is estimated to be $I_{zpf} \approx 44$ nA. This value is used to simulate the corresponding three-dimensional distribution of the vacuum magnetic field $\mathbf{b_0}$, within the volume of the ruby sample. The magnetic field maps of the three components $b_0^{x_0}$, $b_0^{y_0}$ and $b_0^{z_0}$ are shown in Supplementary Fig. 2 for both angles, along with the evolution of the field with y_0 at some characteristic locations within the resonator. From this distribution, we calculate the matrix element in Eq. (4), $\langle \phi_k | b_0^x(\mathbf{r_i})S_x + b_0^y(\mathbf{r_i})S_y + b_0^z(\mathbf{r_i})S_z | \phi_l \rangle$ for each spin at location $\mathbf{r_i}$. Supplementary Fig. 3 provides examples of maps of the local spin-photon coupling. The effective coupling constant $\bar{\Omega}$ at a given temperature is then obtained for the six ESR transitions by summing the contributions of the spins within the volume of the ruby sample, assuming a uniform spin density $n = 0.05\%$. Additional details on the simulation and calculation of $\bar{\Omega}$ are provided in the Supplementary Note 2. A comparison between the theoretical predictions and the coupling constants experimentally determined is shown in Fig. 6a (θ_1) and Fig. 6b (θ_2). An excellent agreement is obtained in the entire

temperature range for all the transitions. The only adjustment parameter is a small shift δy_0 in the vertical position of the ruby sample, which affects the absolute value of $\bar{\Omega}$ through the $\mathbf{b_0}$ magnetic field distribution inside the ruby[46]. This shift accounts for the thin glue layer that holds the sample on the resonator chip. In a first-order approximation, one can consider that for a fixed angle θ, this shift corresponds to a global scaling factor that affects all the transitions the same way.

According to Eq. (4), the amplitude of the coupling constant for the different transitions, as well as their temperature dependencies, is controlled by the transition matrix element and the thermal polarization factor $n_{kl}(T)$, which is shown for all transitions in Supplementary Fig. 3. For temperatures above 10K, where $E_{i=3,4} - E_1 \ll k_B T$, all energy levels are nearly equally populated, resulting in a small polarization factor $n_{kl}(T)$ for all transitions. As the temperature decreases, the coupling for the transitions $T_{2a}^{\theta_1}$ ($E_2 \Leftrightarrow E_3$), $T_{2b}^{\theta_1}$ ($E_2 \Leftrightarrow E_3$), and $T_3^{\theta_{1,2}}$ ($E_3 \Leftrightarrow E_4$), which occur between excited states, exhibit a non-monotonic evolution due to the interplay of two opposing processes. Cooling first increases the relative occupation difference between the energy levels, leading to an increase in $n_{kl}(T)$. Nevertheless, at lower temperatures, the occupation of the excited states eventually decreases to zero and the ground state is solely populated, resulting in $n_{23}(T) \rightarrow 0$ and $n_{34}(T) \rightarrow 0$, while $n_{12}(T) \rightarrow 1$. Consequently, the $T_{2a}^{\theta_1}$, $T_{2b}^{\theta_1}$, and $T_3^{\theta_{1,2}}$ transitions disappear, whereas the transition $T_1^{\theta_{1,2}}$ ($E_1 \Leftrightarrow E_2$) between the ground state and the first excited state is favored, in particular when $k_B T < \hbar \omega_0$. However, at angle θ_1, the coupling remains weak for this transition due to the very small value of the transition matrix element $\langle \phi_1 | W | \phi_2 \rangle$ (Fig. 4a). Indeed, for small magnetic fields, the $|\phi_1\rangle$ and $|\phi_2\rangle$ states mainly retain their $|3/2\rangle$ and $|-3/2\rangle$ state character, respectively, as indicated by the green and red colors in Fig. 2b. According to the selection rule $\Delta m = \pm 1$, these states do not contribute to the transition. In contrast, at angle θ_2 (Fig. 4b), the stronger hybridization significantly increases the transition matrix element $\langle \phi_1 | W | \phi_2 \rangle$, resulting in an enhanced spin-cavity coupling, up to 21 MHz. As seen above in Eq. (4), the effective spin-photon coupling increases as the square root of the total number of spins. It is therefore possible to define an average coupling per spin Ω_s, considering the simple relation $\bar{\Omega} = \Omega_s \sqrt{N}$. Our sample includes a total number of spin $N \approx 2.6 \times 10^{15}$ spins, which corresponds to $\Omega_s/2\pi \approx 0.41$ Hz. However, the contribution of an individual spin decreases with lateral and vertical distance from the resonator due to the decay of the microwave field. As a result, only a fraction of the spins make a significant contribution to the coupling, primarily those located in the regions near the resonator, as seen in Supplementary Figs. 2 and 3. If we consider only the spins located within a volume where the $\mathbf{b_0}$ field reaches at least 10% of its maximum value, the estimated average coupling per spin increases to 1.25 Hz.

Conclusion

In conclusion, we employed electron spin resonance (ESR) techniques to measure the coupling strength between a Cr^{3+} $S = 3/2$ spin ensemble in a ruby crystal and a quantized electromagnetic mode of a high-T_c superconducting cavity across an extended range of temperatures and magnetic fields. We complemented our experimental findings with a theoretical analysis within the Tavis–Cummings model framework, simulating the spatial distribution of the magnetic field generated by the zero-point fluctuations in the cavity and summing the contribution of individual spins to the effective spin-cavity coupling. The results showed a strong agreement between theory and experiment, revealing a complex, temperature-dependent coupling driven by the interplay of thermal polarization and quantum transition probabilities. Additionally, by adjusting the magnetic field orientation relative to the crystal axis, we demonstrated control over the number of active transitions in the quantum system. This work demonstrates the potential of high-spin systems for quantum information processing, particularly in leveraging ESR techniques for spin-state manipulation. Although the present experiment does not reach the strong coupling regime necessary for direct quantum information applications, our methodology provides a valuable framework for studying spin-photon interactions. Future research focusing on optimizing spin-cavity coupling

and exploring alternative spin ensembles with longer coherence times, such as NV centers or rare earth ions, will be crucial for advancing the role of high-spin systems in quantum technologies.

Methods

Sample fabrication and microwave cryogenic setup

In this study, we used distributed $\lambda/2$ - coplanar waveguide cavities fabricated from a 200 nm thick commercial $YBa_2Cu_3O_{7-\delta}$ thin film, provided by Ceraco GmbH ($T_c \simeq 88$ K). The film was grown on a sapphire substrate with a CeO_2 buffer layer and protected by a 20 nm thick Au layer. The cavity structure was defined by Ar ion beam etching through an AZ5214 optical resist, patterned using laser lithography. Alternatively, selective amorphization of the $YBa_2Cu_3O_{7-\delta}$ layer via high-energy ion implantation could advantageously replace the etching step[47–50]. Finally, additional Ti/Au contact pads were deposited through lift-off, followed by the removal of the protective gold layer. The cavity features a central conductor 60 μm wide, separated from two lateral ground planes by a 30 μm gap. The properties of such devices have been reported in ref. 31. The cavity was then integrated into a microwave printed circuit board (PCB) with a ruby crystal placed on top of the cavity center, secured using a thin layer of vacuum grease (Fig. 1a). A small amount of DPPH powder, known for its highly stable free radical and common used as a reference $S = 1/2$ spin marker in ESR spectroscopy, was also deposited on the chip. The assembly was cooled down in a dilution refrigerator equipped with a 7 T superconducting magnet to produce an in-plane Zeeman magnetic field B (Fig. 1a). The microwave signal was coupled to the cavity through an approximately 50 dB attenuated line and the transmitted signal was amplified at the 3 K stage by a low noise cryogenic HEMT amplifier. Two isolators, placed at the mixing chamber and 3 K stages, were used to minimize back-action noise on the device. The transmission $S_{21}(\omega)$ was recorded using a Vector Network Analyzer. All the experiments were performed with a microwave power $P_{in} \approx -65$ dBm at the input of the cavity. The corresponding average photon number in the cavity is given by $\bar{n} = 2P_{in}Q^2/(\hbar\omega_0^2 Q_c) \approx 2 \times 10^6$, where $Q_c \approx 180,000$ is the coupling quality factor[31].

Data availability

The authors declare that the data that support the findings of this study are available within the article. All other relevant data are available from the corresponding authors upon request.

References

1. Nielsen, M. A. & Chuang, I. L. *Quantum Computation and Quantum Information* (Cambridge Univ. Press, 2000).
2. Kurizki, G. et al. Quantum technologies with hybrid systems. *Proc. Natl Acad. Sci. USA* **112**, 38663873 (2015).
3. Morton, J. J. L. & Bertet, P. Storing quantum information in spins and high-sensitivity ESR. *J. Magn. Reson.* **287**, 128139 (2018).
4. Fuchs, G. D., Burkard, G., Klimov, P. V. & Awschalom, D. D. A quantum memory intrinsic to single nitrogenvacancy centres in diamond. *Nat. Phys.* **7**, 789793 (2011).
5. Lai, Y.-Y., Lin, G.-D., Twamley, J. & Goan, H.-S. Single-nitrogen-vacancy-center quantum memory for a superconducting flux qubit mediated by a ferromagnet. *Phys. Rev. A* **97**, 052303 (2018).
6. Morello, A., Pla, J. J., Bertet, P. & Jamieson, D. N. Donor spins in silicon for quantum technologies. *Adv. Quantum Technol.* **3**, 2000005 (2020).
7. Hedges, M. P., Longdell, J. J., Li, Y. & Sellars, M. J. Efficient quantum memory for light. *Nature* **465**, 10521056 (2010).
8. O'Brien, C., Lauk, N., Blum, S., Morigi, G. & Fleischhauer, M. Interfacing superconducting qubits and telecom photons via a rare-Earth-doped crystal. *Phys. Rev. Lett.* **113**, 063603 (2014).
9. Imamoglu, A. Cavity QED based on collective magnetic dipole coupling: spin ensembles as hybrid two-level systems. *Phys. Rev. Lett.* **102**, 083602 (2009).
10. Wesenberg, J. H. et al. Quantum computing with an electron spin ensemble. *Phys. Rev. Lett.* **103**, 070502 (2009).
11. Wang, Y., Hu, Z., Sanders, B. C. & Kais, S. Qudits and high-dimensional quantum computing. *Front. Phys.* **8**, 479 (2020).
12. Bullock, S. S., O'Leary, D. P. & Brennen, G. K. Asymptotically optimal quantum circuits for d-level systems. *Phys. Rev. Lett.* **94**, 230502 (2005).
13. Blok, M. S. et al. Quantum information scrambling on a superconducting qutrit processor. *Phys. Rev. X* **11**, 021010 (2021).
14. Champion, E., Wang, Z., Parker, R. & Blok, M. Efficient control of a transmon qudit using effective spin-7/2 rotations. *Phys. Rev. X* https://doi.org/10.1103/vbh4-lysv (2025).
15. Ringbauer, M. et al. A universal qudit quantum processor with trapped ions. *Nat. Phys.* **18**, 1053–1057 (2022).
16. Jenkins, M. D. et al. Coherent manipulation of three-qubit states in a molecular single-ion magnet. *Phys. Rev. B.* **95**, 064423 (2017).
17. Godfrin, C. et al. Operating quantum states in single magnetic molecules: implementation of Grover's quantum algorithm. *Phys. Rev. Lett.* **119**, 187702 (2017).
18. Dolde, F. et al. High-fidelity spin entanglement using optimal control. *Nat. Commun.* **5**, 3371 (2014).
19. Asaad, S. et al. Coherent electrical control of a single high-spin nucleus in silicon. *Nature* **579**, 205209 (2020).
20. Wolfowicz, G. et al. Atomic clock transitions in silicon-based spin qubits. *Nat. Nanotechnol.* **8**, 561564 (2013).
21. Wolfowicz, G. et al. Coherent storage of microwave excitations in rare-earth nuclear spins. *Phys. Rev. Lett.* **114**, 170503 (2015).
22. Blais, A., Grimsmo, A. L., Girvin, S. M. & Wallraff, A. Circuit quantum electrodynamics. *Rev. Mod. Phys.* **93**, 025005 (2021).
23. Krantz, P. et al. A quantum engineer's guide to superconducting qubits. *Appl. Phys. Rev.* **6**, 021318 (2019).
24. Schuster, D. I. et al. High-cooperativity coupling of electron-spin ensembles to superconducting cavities. *Phys. Rev. Lett.* **105**, 140501 (2010).
25. Kubo, Y. et al. Strong Coupling of a spin ensemble to a superconducting resonator. *Phys. Rev. Lett.* **105**, 140502 (2010).
26. Yu, C. X. et al. Magnetic field resilient high kinetic inductance superconducting niobium nitride coplanar waveguide resonators. *Appl. Phys. Lett.* **118**, 054001 (2021).
27. Ghigo, G. et al. Vortex dynamics in NbTi films at high frequency and high DC magnetic fields. *Sci. Rep.* **13**, 9315 (2023).
28. Borisov, K. et al. Superconducting granular aluminum resonators resilient to magnetic fields up to 1 Tesla. *Appl. Phys. Lett.* **117**, 120502 (2020).
29. Ghirri, A. et al. $YBa_2Cu_3O_7$ microwave resonators for strong collective coupling with spin ensembles. *Appl. Phys. Lett.* **106**, 184101 (2015).
30. Ghirri, A. et al. Coherently coupling distinct spin ensembles through a high-Tc superconducting resonator. *Phys. Rev. A* **93**, 063855 (2016).
31. Velluire-Pellat, Z. et al. Hybrid quantum systems with high-Tc superconducting resonators. *Sci. Rep.* **13**, 14366 (2023).
32. Tavis, M. & Cummings, F. W. Exact solution for an N-molecule-radiation-field Hamiltonian. *Phys. Rev.* **170**, 379 (1968).
33. Tavis, M. & Cummings, F. W. Approximate solutions for an N-molecule-radiation-field Hamiltonian. *Phys. Rev.* **188**, 692 (1969).
34. Maiman, T. H. Stimulated optical radiation in ruby. *Nature* **187**, 493494 (1960).
35. Makhov, G., Kikuchi, C., Lambe, J. & Terhune, R. W. Maser action in ruby. *Phys. Rev.* **109**, 1399 (1958).
36. Clauss, C. et al. Broadband electron spin resonance from 500 MHz to 40 GHz using superconducting coplanar waveguides. *Appl. Phys. Lett.* **102**, 162601 (2013).

37. Zmuidzinas, J. Superconducting microresonators: physics and applications. *Annu. Rev. Condens. Matter Phys.* **3**, 169214 (2012).

38. Manenkov, A. A. & Prokhorov, A. M. The fine structure of the spectrum of the paramagnetic resonance of the ion Cr^{3+} in chromium corundum. *Sov. Phys. JETP* **1**, 610 (1955).

39. Geusic, J. E. Paramagnetic fine structure spectrum of Cr^{3+} in a single ruby crystal. *Phys. Rev.* **102**, 1252 (1956).

40. Kikuchi, C., Lambe, J., Makhov, G. & Hamilton, W. O. Ruby as a maser material. *J. Appl. Phys.* **30**, 10611065 (1959).

41. Jaynes, E. T. & Cummings, F. W. Comparison of quantum and semiclassical radiation theories with application to the beam maser. *Proc. IEEE* **51**, 89109 (1963).

42. Jenkins, M. et al. Coupling single-molecule magnets to quantum circuits. *New J. Phys.* **15**, 095007 (2013).

43. Dicke, R. H. Coherence in spontaneous radiation processes. *Phys. Rev.* **93**, 99 (1954).

44. Clerk, A. A., Devoret, M. H., Girvin, S. M., Marquardt, F. & Schoelkopf, R. J. Introduction to quantum noise, measurement, and amplification. *Rev. Mod. Phys.* **82**, 1155 (2010).

45. Göppl, M. et al. Coplanar waveguide resonators for circuit quantum electrodynamics. *J. Appl. Phys.* **104**, 113904 (2008).

46. Rollano, V. et al. High cooperativity coupling to nuclear spins on a circuit quantum electrodynamics architecture. *Commun. Phys.* **5**, 246 (2022).

47. Malnou, M. et al. High-T_c superconducting Josephson mixers for terahertz heterodyne detection. *J. Appl. Phys.* **116**, 074505 (2014).

48. Amari, P. et al. High-temperature superconducting nanomeanders made by ion irradiation. *Supercond. Sci. Technol.* **31**, 015019 (2018).

49. Amari, P. et al. Scalable nanofabrication of high-quality $YBa_2Cu_3O_7$ nanowires for single photon detectors. *Phys. Rev. Appl.* **20**, 044025 (2023).

50. Couëdo F. et al. High-T_c superconducting detector for highly-sensitive microwave magnetometry. *Appl. Phys. Lett.* **114**, 192602 (2019).

Acknowledgements

Author contributions

Samples were fabricated by Z.V.-P. and C.F.-P. Z.V.-P. performed the measurements with the help of E.M. and carried out the analysis of the data under the supervision of N.B. and with inputs from all the authors. Z.V.-P. and N.B. wrote the manuscript.

Competing interests

The authors declare no competing financial interests.

Additional information

Supplementary information The online version contains supplementary material available at https://doi.org/10.1038/s42005-025-02159-1.

Correspondence and requests for materials should be addressed to N. Bergeal.

Reprints and permissions information is available at http://www.nature.com/reprints

Publisher's note Springer Nature remains neutral with regard to jurisdictional claims in published maps and institutional affiliations.